minerals

MDPI

Article

Experimental and Simulation Studies on the Mn Oxidation State Evolution of a Li_2O-MnO_x-CaO-SiO_2 Slag Analogue

Sven Hampel [1,†], Iyad Alabd Alhafez [2], Alena Schnickmann [3], Sophie Wunderlich [1], Haojie Li [4], Michael Fischlschweiger [4], Thomas Schirmer [3], Nina Merkert [2] and Ursula E. A. Fittschen [1,*]

[1] Institute of Inorganic and Analytical Chemistry, Clausthal University of Technology, Arnold-Sommerfeld-Str. 4, 38678 Clausthal-Zellerfeld, Germany; sven.hampel@tu-clausthal.de (S.H.); sophie.wunderlich@tu-clausthal.de (S.W.)
[2] Institute of Applied Mechanics, Clausthal University of Technology, Arnold-Sommerfeld-Str. 6, 38678 Clausthal-Zellerfeld, Germany; iyad.alabd.alhafez@tu-clausthal.de (I.A.A.); nina.merkert@tu-clausthal.de (N.M.)
[3] Institute of Repository Research, Clausthal University of Technology, Adolph-Roemer-Str. 2A, 38678 Clausthal-Zellerfeld, Germany; alena.schnickmann@tu-clausthal.de (A.S.); thomas.schirmer@tu-clausthal.de (T.S.)
[4] Institute of Energy Process Engineering and Fuel Technology, Clausthal University of Technology, Agricolastr. 4, 38678 Clausthal-Zellerfeld, Germany; haojie.li@tu-clausthal.de (H.L.); michael.fischlschweiger@tu-clausthal.de (M.F.)
* Correspondence: ursula.fittschen@tu-clausthal.de; Tel.: +49-5323-72-2205
† Current address: Centre for X-ray and Nano Science, Deutsches Elektronen-Synchrotron, Notkestr. 85, 22607 Hamburg, Germany.

Abstract: This manuscript presents the results from the synthesis and characterization of a slag analogue with a nominal composition of 17 wt% $LiMnO_2$ and 83 wt% Ca_2SiO_4 encountering fairly high cooling rates in order to study the evolution of Mn-species. The Mn species was also simulated from 1223 K to 1773 K using a thermodynamic model, assuming a homogeneous melt. The micro-composition including the Mn species of the solidified slag was determined experimentally, and was used as basis for molecular dynamics (MD) simulation. The MD simulation provides information on structure and viscosity at high temperatures, which are otherwise difficult to access. These parameters significantly influence oxidation state of redox-active elements and the solidified product. The micro-composition analyzed by electron probe micro analysis (EPMA) and synchrotron-based micro-X-ray fluorescence (micro-XRF) showed that Mn-rich and Ca-Si-rich phases are separated. While the Mn-O phases did not contain noticeable Ca, the Ca_2SiO_4 phase had incorporated 0.6 wt% of Mn. The slag solidified into round-shaped and droplet-shaped grains of a Li-Mn-oxide, some Mn_3O_4 and Ca_2SiO_4. The powder X-ray diffraction (PXRD) confirmed the formation of larnite; the identity of the Li-Mn-oxide, however, remained inconclusive. The Mn oxidation state (OS) was identified using synchrotron-based micro-X-ray absorption near edge spectroscopy (micro-XANES). The Mn-O grains matched well with Li-Mn-oxides and a Mn OS: +3, e.g., $LiMn^{3+}O_2$. Small areas matching hausmannite ($Mn^{2+}Mn_2{}^{3+}O_4$) were also identified. The OS of Mn in the silicate phase could not be identified. For comparison, a slowly cooled slag analogue with similar composition, but higher Si content, was also subjected to micro-XANES. The slowly cooled slag formed long Mn-rich needles in a matrix of large calcium silicate crystals. The Mn-rich crystals matched well with the XANES spectrum of a Mn^{3+} Li-oxide like $LiMn^{3+}O_2$. At the rim of the needles, the Mn-spectra matched well the hausmannite ($Mn^{2+}Mn_2{}^{3+}O_4$) reference. In the silicate phases, Mn had an OS: +2, unambiguously. The melt structure at different temperatures of two compositions, i.e., $LiMn^{3+}O_2$ and Ca_2SiO_4, was simulated using molecular dynamics (MD). They serve as model compositions, assuming a heterogeneous melt. The results show significant different degrees of polymerization and viscosity. Information from MD simulations can support the identification of potentially different oxygen permeability and with that prediction of oxidation states. The bulk composition was identified by inductively coupled plasma optical emission spectrometry (ICP-OES), bulk structure by PXRD and bulk species by lab-XANES. The synchrotron micro analysis including micro-XRD were performed at

check for updates

Citation: Hampel, S.; Alhafez, I.A.; Schnickmann, A.; Wunderlich, S.; Li, H.; Fischlschweiger, M.; Schirmer, T.; Merkert, N.; Fittschen, U.E.A. Experimental and Simulation Studies on the Mn Oxidation State Evolution of a Li_2O-MnO_x-CaO-SiO_2 Slag Analogue. *Minerals* **2024**, *14*, 868. https://doi.org/min14090868

Academic Editors: Rajesh Kumar Jyothi and Mark I. Pownceby

Received: 3 June 2024
Revised: 31 July 2024
Accepted: 23 August 2024
Published: 26 August 2024

the microfocus beamline I18 at the Diamond Light Source. Pure reference compounds were prepared and characterized with the same multi-modal approach.

Keywords: engineered artificial minerals (EnAM); lithium battery recycling; XANES; EPMA; molecular dynamic simulation

1. Introduction

Tailoring metallurgical slags to facilitate an optimal production of a high quality metallic product has been a topic of research and development for a long time [1,2]. In recent years, interest rose to tailor slags to produce recoverable compounds that incorporate critical elements. Materials and elements are considered critical when they are highly important for the economy and their supply security is easily jeopardized. The recoverable synthesized slag compounds are sometimes referred to as engineered artificial minerals (EnAM). The recovery of lithium from Li-ion battery recycling slags in form of a scavenger compound has been studied by, e.g., Elvert et al. [3]. The early crystallizing $LiAlO_2$ was identified as a promising EnAM, and it was shown that it can be separated from gehlenite $Ca_2Al[AlSiO_7]$ using froth flotation obtaining a recovery of 88% [4]. Wittkowski et al. [5] have shown that, with rising concentrations of Mn (approx. 7%), the yield of $LiAlO_2$ decreases, and Li is incorporated into Mn-Al-oxide spinel solid solutions. Schnickmann et al. suggested Li-Mn-oxides as alternative EnAM in the Li_2O-SiO_2-CaO-MnO_n-(MgO)-(Al_2O_3) system. They found that if Al is excluded from the system, Li is incorporated nearly completely in early crystallizing $LiMnO_2$ [6]. The oxidation state of Mn in these artificial slags, produced in ambient air, was determined to be mainly +3. From thermodynamic calculations by Longo et al. [7], it can be deducted that Mn in an oxidation state +4 in form of Li_2MnO_3 is even stabilized in the presence of Al, which emphasizes the importance of understanding how the Mn oxidation state is controlled.

With respect to the studied system, it can be concluded that, besides Mn, none of the metal ions may act as reducer or oxidizer, leaving gases like O_2 and CO as redox-reactive species. The concentration of O_2 in the melt will depend on the temperature, with high temperatures supporting the gas phase and its permeability in general. Mainly, two processes influencing the permeability of O_2 in slags have been discussed, which are the viscosity [2,8], and the reactive dissolution of oxygen by reacting with reduced metal species like Fe^{2+} [9]. A fluid melt enables oxygen diffusivity, while high temperatures favor higher O_2 concentrations in the gas phase. The viscosity depends on the composition of the melt, and can be estimated with the concepts of identifying the relation of network former and network modifier. Silicon and Al are considered network formers, while Li, Ca, and Mn are considered network modifiers [2]. For the Li-ion recycling slag system, the SiO_2 fraction is approx. 20 mol%, and a degree of polymerization, being Q = 2.7 (four highest degrees and zero lowest degrees of polymerization), was calculated. The Q value is obtained from Q = 4-NBO/T, and can be considered as the average of the Q^n structural units.

Making use of the thermodynamic data oxygen equilibrium between the liquid and gas phase can be described. The Calculation of Phase Diagrams (Calphad) method [10] combines different experimental data, such as thermal, caloric properties and phase diagram information, as well as ab initio data to develop thermodynamic databases for predicting materials' phase behavior. This is of particular importance for, e.g., understanding solidification and phase formation. Nowadays, this method is also widely applied to Li-containing oxide material systems to predict respective phase diagrams and solidification [11–16]. The commercial databases FToxide and FactPS [13] can be used to understand and predict heterogeneous phase behaviors considering gas, liquid, and solid phases, and composition during equilibrium solidification. It can be applied to understand the temperature-dependent variation in manganese valence in the liquid slag in relation to the O_2 dissolved in the melt.

The viscosity of a certain composition present in an in-homogeneous melt (in-homogeneous, e.g., because of liquid–liquid and solid–liquid phase separation) can be derived describing the compounds on an atomistic level using molecular dynamic simulations. This has the advantage that the viscosity at any temperature from above to below the liquidus, and even at very high temperatures, is accessible. The degree of polymerization can also be determined. Molecular modeling allows us to investigate the elemental interaction of various elements in a molten state and obtain the RDFs and mean square displacements (MSD). MD simulations are based on Newton's equations of motion, which are solved by so-called integrators. The forces are calculated from interatomic interaction potentials. Further essential components of an MD simulation are the choice of the time step and the definition of the boundary conditions, e.g., by thermostats or barostats. In a post-processing step, the element coordination, viscosity, and network formation in the melt can be determined. The influence of parameters like temperature or concentration gradients can be studied to achieve an efficient slag design, this mostly with respect to an optimal metal product. A recent review is found by Zhou et al. [17]. MD simulations have been frequently used to obtain the short-range ordered structure of molten slags and the melt's kinetic characteristics [18,19]. MD research had focused on the analysis of different slag systems, including silicate slags [20], Al slags [21], and aluminosilicate slags [22,23]. With respect to the lithium EnAM, lithium aluminates have been studied with MD simulations and experimentally. Individual diffusivities depend on the Li:Al ratio, and strongly decrease viscosity [24]. The effect of Mn has been less explored. The network breaking properties of MnO in Al_2O_3-SiO_2-CaO-MnO slags were described using MD simulation [19].

The composition of the melt is fundamental for the macroscopic properties. Major challenges for obtaining the accurate composition when the Mn species is formed are the uncertainties on local gradients. The local composition is affected by phase separations; these are solid–liquid (SL) separations but also liquid–liquid (LL) and gas–liquid (GL) separations. The local composition may encounter sharp boundaries if LL-phase separation occurs and there are compositional gradients while the solidification proceeds. These gradients can be described incrementally from systems with reduced complexity. This has been performed for $LiAlO_2$ and for the thermodynamically predicted compounds sharing its precipitation zone, which are $LiAl_5O_8$ spinel and Li_5AlO_4 [24], and a recent review paper describes this approach [25]. In this work, the Li_2O-MnO_x-SiO_2-CaO system is studied. The slag analogue, which had encountered fairly steep cooling rates during its genesis, showed a separation of Si-Ca and Mn-rich phases with the Si-Ca phases containing minor amounts of Mn. The shape of the separated phase is round and in case of the Mn-rich compounds droplet shaped. The Mn species of the micro-compounds was characterized using micro-XANES strongly supporting the Mn-rich compounds being Li-Mn^{3+} oxides. As the concentration of Mn in the Si-Ca phase was very low, a slowly cooled slag analogue of the same system was also studied. Two compounds representing the Li-Mn-O and the Ca-Si-O phases were studied separately with MD simulations at high temperatures, and the individual viscosity was determined. Future simulations will need to included minor elements present in the micro-compounds, to move closer to the description of the real system.

2. Materials and Methods

2.1. Molecular Dynamic Simulations

All of the molecular dynamics simulations are performed with the open-source LAMMPS code [26]. In all simulations, time steps of 1 fs were chosen with periodic boundary conditions. In the slag analogue, mostly calcium silicate Ca_2SiO_4 and a lithium manganate(III) were present; hence, larnite and $LiMnO_2$ were studied by charged particle interactions. They are described by the long-range Coulomb and the short-range Buckingham potential (Equation (1)):

$$V_{ij} = \frac{1}{4\pi\varepsilon_0}\frac{q_i q_j}{r_{ij}} + \left[A_{ij}\exp\left(\frac{-r_{ij}}{\rho_{ij}}\right) - \frac{C_{ij}}{r_{ij}^6}\right] \quad (1)$$

Here, i and j denote an interacting pair of two ions among the present elements separated by a distance r_{ij}, and ε_0 stands for the dielectric constant. The Buckingham potential parameters are taken from Cormack and Du [27], as well as Sayle et al. [28], and are listed in Table 1.

Table 1. Interatomic potential parameters used in the atomistic simulations of the Li-Mn-O system (**top**) and Ca-Si-O system (**bottom**). The values are given rounded to the same number of digits for each column.

Interaction	A (eV)	ρ (Å)	C (eV Å^6)	Charge
Li^+–Li^+	270,000	0.143	0.00	0.55
Li^+–Mn^{3+}	0	0.000	0.00	
Li^+–O^{2-}	30,000	0.154	0.00	
Mn^{3+}–Mn^{3+}	33,884	0.156	16.00	1.65
Mn^{3+}–O^{2-}	18,646	0.195	22.00	
O^{2-}–O^{2-}	11,783	0.234	30.22	–1.10
Ca^{2+}–Ca^{2+}	10,000	0.230	0.00	1.20
Ca^{2+}–Si^{2+}	0	0.000	0.00	
Ca^{2+}–O^{2-}	1,314,000	0.187	60.00	
Si^{4+}–Si^{4+}	0	0.000	0.00	2.40
Si^{4+}–O^{2-}	180,046	0.205	133.54	
O^{2-}–O^{2-}	1389	0.362	175.00	–1.20

The crystal structure of both compounds at the initial state is summarized in Table 2 and shown in Figure 1. The initial atomic coordinates were taken from [29]. Size effects of the simulated systems are expected to be small, using properly large cells and by applying periodic boundary conditions in all three dimensions. At first, the samples are relaxed at a temperature of around 300 K using an isothermal-isobaric (NPT) ensemble for 20 ps. After relaxation of the samples, the compounds are heated up to the target temperature of 2900 K for Ca_2SiO_4 and 2700 K for $LiMnO_2$. These high temperatures were chosen to ensure that all compounds are in liquid state. At the target temperature, the samples are relaxed again for 1000 ps. All visualizations, as well as the analysis of the radial distribution function and the coordination analysis, are performed by the software tool OVITO-PRO 3.8.0 [30].

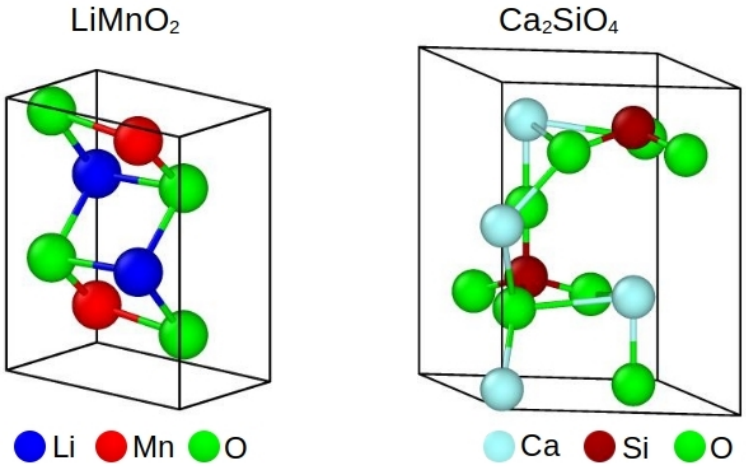

Figure 1. Left: structure of $LiMnO_2$ with Mn (red), Li (blue) and O (green). **Right**: Ca_2SiO_4 with Ca (light blue), Si (red) and O (green).

Table 2. Compounds used in the simulations, their crystal systems, space groups, dimensions and the number of atoms.

Compound	Crystal System	Space Group	Volume (Å^3)	Number of Atoms
$LiMnO_2$	Orthorhombic	Pmmn	151,165	16,416
Ca_2SiO_4	Hexagonal	$P6_3mc$	202,262	14,112

2.2. Calphad Model

The commercial databases FToxide and FactPS [13] were used for heterogeneous phase behavior and composition during equilibrium solidification. The system considered solid, liquid, and gaseous phases, while the latter are assumed at fixed partial pressures, e.g., oxygen at 0.21 bar. A Modified Quasichemical Model (MQM) was used for the liquid slag [31–33], where the manganese oxidation states Mn(II) and Mn(III) are considered [13]. Solid phases with stoichiometric compounds and solid solutions are also computed based on FToxide and FactPS [13].

2.3. Chemicals

Chemicals were obtained from different suppliers (BASF, Ludwigshafen, Germany; Carl Roth, Karlsruhe, Germany; CWS Chemiewerk Bad Köstritz, Bad Köstritz, Germany; Merck, Darmstadt, Germany) in per analysis grade or better (unless otherwise noted): aluminum nitrate nona hydrate (≥98%), ammonia (25 wt%, technical), ammonium nitrate, calcium hydroxide, citric acid monohydrate, hydrogen peroxide (35 wt%), Köstrosol 0830AS (ammonia stabilized silicon oxide nanoparticles in water, 8 nm, 30 wt%), lithium hydroxide (98%+), manganese(II) oxide, manganese(II/III) oxide, manganese(III) oxide, manganese(IV) oxide, manganese(II) nitrate tetra hydrate (≥98%), nitric acid (65 wt%), potassium bisulfate, and sulfuric acid (98 wt%), and were used for the slag preparation, as well as in the synthesis of references. Dilutions were performed with ultra-pure water (>18.2 MΩ cm, Purelab Flex 4, ELGA Veolia, High Wycombe, UK). Sodium tetra borate and hydrochloric acid (37 wt%) were used for fuse beads, followed by leaching for ICP-OES analysis. Cellulose (micro crystalline, for optical measurements) and poly(imide) foil (Conrad electronic, Hirschau, Germany) were used for XANES pellet preparation.

Glazed porcelain crucibles (15 mL, wide form) were used from IDL for synthesis of the precursor. The crucibles were cleaned in boiling diluted piranha acid, followed by boiling 10 % nitric acid and boiling ultra-pure water (each step for 2 h). At last, a heating step 1273 K for 2 h was performed before usage. The final slag was prepared in platinum rhodium (90/10) crucibles. They were cleaned several times with a melt of potassium bisulfate, followed by rinsing in 10 % nitric acid and ultra-pure water.

2.4. Instrumentation and Measurements

2.4.1. Oven

Sintering of the powders prepared by sol-gel-synthesis yielding the precursor was performed in a Nabertherm L 3/11 furnace with minimal air supply. Synthesis of the final slag was realized in a Naberthem HT 40/17 high temperature furnace.

2.4.2. XANES

Lab X-ray absorption near edge structure analysis (lab-XANES) was performed with an EasyXAFS easyXES100-extended [5,34,35]. The setup composes of a Pd/W X-ray tube (powered at 25 kV/3 mA), a Si(110) spherically bent crystal analyzer, and a Ketek ASAS-M1 silicon drift detector with a helium-filled flight path between all components. Further information about the setup is described in the literature [34,35]. Evaluation was performed with custom Python scripts following the ATHENA package [36]. Energy calibration was performed with a manganese foil (ExafsMaterials, Danville, CA, USA), according to Wittkowski et al. [5]. The energy range is set to 6482–6739 eV (ΔE = 0.25 eV, t = 2 s) and 6739–6899 eV (ΔE = 1 eV, t = 1 s), resulting in approx. 40 min per measurement. Each

specimen is measured at least six times with the same number of I_0 measurements (80 mg pellet of pure cellulose).

The specimens were prepared as pellets (16 mm diameter) encapsulated in poly(imide) foil, consisting of up to 20 mg of sample with 80 mg cellulose. References were chosen according to the possible presence in the slags and include manganese(II) oxide MnO, manganese(II/III) oxide Mn_3O_4 (hausmannite), manganese(III) oxide Mn_2O_3, manganese(IV) oxide MnO_2, as well as galaxite $MnAl_2O_4$, lithium manganate(III) $LiMnO_2$, lithium manganate(III/IV) $LiMn_2O_4$, and lithium manganate(IV) Li_2MnO_3. The latter were prepared by sol gel combustion with the same procedure as for the slag, or by the procedure described by Wittkowski et al. [5].

2.4.3. PXRD

Powder X-ray diffraction analysis (PXRD) was performed with a PANalytical X-Pert Pro diffractometer with Co Kα excitation (λ = 1.789 Å, 40 kV, 40 mA) as backloading sample in Bragg–Brentano geometry. Identification of the phases was evaluated with the PDF-2 ICDD database [37]. Rietveld refinement/Le Bail fit was performed with the program package Fullprof [38].

2.4.4. EPMA

A Cameca SX^{FIVE} FE Field Emission was used for electron probe micro analysis (EPMA), consisting of single crystals with elemental determination and back scattered electron detection. Wavelength dispersive quantification was performed for Na Kα, Mg Kα, Al Kα, Si Kα, Ca Kα, and Mn Kα. Certified reference materials (PandH Developments and Astimex Standards) were used for calibration. Free-standing thin sections of the corresponding samples were coated with a carbon layer before measurements at 15 kV at smallest beam size (100–600 nm, Schottky type [39]). Typical limits of detection (LOD) are determined for this sample system, with 100 ppm for Ca Kα and Al Kα, 140 ppm for Mg Kα and Si α), 230 ppm for Na Kα, and 1150 ppm for Mn Kα. Visualization of the raw data were achieved by the peaksight-binary-parser within the HussariX package by Jokubauskas [40].

2.4.5. ICP-OES

Fuse beads were prepared by mixing 100 mg sample with 2.5 g sodium tetra borate and subsequent heating to 1323 K for 20 min. The beads were leached with diluted hydrochloric acid, and filled to 200 mL final volume. The stock solutions were diluted 1:20 for ICP-OES measurement performed with an Agilent ICP-OES 5100 (Santa Clara, CA, USA), as well as a Varian Vista-MPX evaluating Li 670.78 nm, Al 396.15 nm, Ca 422.67 nm, Mg 279.55 nm, Mn 257.61 nm, Si 251.61 nm, and Pt 214.42 lines. The matrix-adapted external calibration (10 $\mu g \cdot L^{-1}$–10 $mg \cdot L^{-1}$) was performed using blank preparations. Each sample was analyzed in two replicates. The limits of detection (LOD) were determined considering three times the residual standard deviation divided by the slope of the calibration.

2.4.6. CHNS

Elemental analysis (CHNS) of the precursors was performed with an Elementar varioMICRO (Langenselbold, Germany) CHNS with four replicates per sample (about 3 mg per run). Elemental analysis (CHNS) yielded 5.6 $\pm$ 0.2 wt% nitrogen, as well as minor fractions of 0.5 $\pm$ 0.2 wt% hydrogen, and 0.19 $\pm$ 0.03 wt% carbon.

2.4.7. Micro-XRD, -XRF and XANES

Micro analysis on the thin sections was performed at the Diamond Light Source on end station I18 [41]. The beam was focused with Kirkpatrick–Baez mirrors to a 2 $\times$ 2 µm spot size. The energy resolution is given with $\Delta E/E = 1.4 \times 10^{-4}$ by a Si(110) double crystal monochromator. Data acquisition was performed with a Vortex-ME4 silicon drift detector (1 mm thickness) for XRF, an Excalibur area detector (115 $\times$ 100 mm active area) for XRD, and an ionization chamber for the photon flux. Calibration of the XRD area detector

was performed with lanthanum boride LaB_6 powder sample, while energy calibration for XANES is determined with a Mn foil (Goodfellow Cambridge, Huntingdon, UK). Reference spectra were measured using the same pellets from lab-XANES with 10 × 10 µm area scans for better statistics. Micro-XRF and micro-XRD were determined at 18 keV with a dwell time of 0.1 s per point. Micro-XANES in fluorescence mode was performed at the Mn K-edge with the following energy regions: 6500–6538 eV (ΔE = 9.5 eV), 6540.25 eV, 6542–6557.5 eV (ΔE = 0.5 eV), and 6560–6800 eV (ΔE = 50 eV). For each energy, 2D scans were obtained with a dwell time of 0.5 s per point. The linear combination fits of the normalized XANES spectra were performed in the region 6538–6537 eV. Data evaluation included the usage of DAWN [42,43] for micro-XRF/XRD, MANTiS and TXM Wizard for micro-XANES [44,45], and PyFAI for micro-XRD processing and calibration [46,47].

2.5. Slag Analogue Preparation

Borosilicate beakers (1 L, high shape) and glazed porcelain crucibles were cleaned with 40 wt% sulfuric acid/6 wt% hydrogen peroxide for 2 h at reflux, followed by 10 wt% nitric acid for 2 h at reflux, and ultra-pure water for 2 h at reflux. Between each cleaning step, multiple rinsings with ultra-pure water were performed.

In a 1 L borosilicate beaker, 0.323 g lithium hydroxide, 2.707 g calcium hydroxide, and 1.690 g manganese(II) nitrate tetra hydrate were dissolved in 50 mL 30% nitric acid. Afterwards, 15.761 g of citric acid mono hydrate were added under heating to reflux. At reflux, the pH value was adjusted to about 6 with 25% ammonia. Excess water was removed by boiling until the mixture thickened to a syrup, followed by the addition of 3.1 mL Köstrosol 0830AS. With the heating plate set to maximum (723 K), the mixture was heated until self ignition set in. If combustion was not fully obtained, about 5 g of ammonium nitrate and 10 mL of ultra-pure water were added to the cooled beaker, followed by another ignition procedure. The total amount of substances was set to 75 mmol, requiring two to three ignition steps, compared to a 25 mmol total amount of substances using only one combustion step [24]. The sol-gel combustion was prepared four times. resulting in 28.84 g powder. The powder was finely ground with 21.77 g ammonium nitrate before heating the mixture in three portions up to 753 K, yielding 10.62 g of precursor.

The slag preparation was performed in duplicate with 3 g of precursor in platinum rhodium (90/10) crucibles up to a temperature of 1673 K. The heating program was adapted according to earlier studies [5,6,15] comprising the following temperature steps: 298 K to 323 K (0.21 $K \cdot min^{-1}$, 2.5 h holding time), 323 K to 993 K (2.8 $K \cdot min^{-1}$), 993 K to 1573 K (2.3 $K \cdot min^{-1}$, 2 h holding time), after cooling to ca. 1173 K (about 4.4 $K \cdot min^{-1}$), and a final heating to 1673 K was set (25 $K \cdot min^{-1}$, 0.75 h holding time).

The liquid slags were extracted from the furnace at 1673 K and poured onto a steel plate, resulting in a fast-cooling yielding 2.013 g (run A) and 2.135 g (run B) of the final slag, respectively. The beads were cut in two pieces with (a) one half for free-standing thin film preparation, and (b) the other half for further analysis, which was ground in an agate ball mill to a fine powder. The thin films were prepared on glass substrate with a 3 mm hole for transmission measurements, resulting in a free-standing thin film in that spot. In the following, this is described as fast-cooled slag. A thin film section of a slow-cooled slag with a similar composition was directly used from Schnickmann et al. for microscopic characteristics (micro-XRF and micro-XANES), with its preparation and characterization described earlier [6].

3. Results and Discussion

3.1. Bulk Characteristics of the Solidified Li_2O-MnO_x-SiO_2-CaO

The oxide system studied here represents a simplified slag that may be obtained in Li-ion battery pyrometallurgical recycling. The major elements (Ca and Si, as well as Li) are present. Manganese, as a potential EnAM-forming element, was added in an amount which should allow all of the Li to be bound in a lithium manganate EnAM. Manganese is part of most novel Li-ion battery cathode materials; accordingly, its presence is expected in

the slag. Aluminum, though it is used as current collector and housing material in batteries, was not considered in this synthetic slag, in order to keep the system as simple as possible. Its presence leads to much larger number of compounds [6]. In an actual recycling process, it would be possible to separate housing and collectors prior to the pyrometallurgical procedure. After shredding of the intact cells, mechanical sorting/screening of the crushed residual, e.g., by magnetic separation or zigzag classifiers, will result in several fractions, including housing and collectors [48,49]. The synthesis' aim was to produce a solidified product including fast cooling, having a composition of 2.4 wt% of Li_2O, 9.3 wt% Mn_2O_3, 37.2 wt% CaO and 13 wt% SiO_2. The precursor was prepared by sol-gel-synthesis, leading to a fine powder mixed on a molecular scale to prevent local elemental gradients due to large particles. The bulk composition of the final product was verified by ICP-OES, and yielded, in general, the expected amount; however, there was somewhat less Li and Mn, and more Si and Ca, in two replicates (slag A and B; see Table 3). The comparison of the molar fractions (without carbon, oxygen, nitrogen, and hydrogen) gives information on actual losses, i.e., lithium by about 10 % is found, while the silicon, calcium, and manganese compositions are unaltered (see Table 3). Mass fractions of all elements in the precursor are below the expected values due to presence of nitrogen-bearing compounds, as well as excess oxygen bound in MnO_2. Lithium is known to evaporate at elevated temperatures [50]. Fine homogeneous powders with increased surfaces may enhance the evaporation before melting occurs. Trace elements present in the products were below the limits of detection (LOD) given for Mg (0.63 wt%), Al (0.21 wt%), and Pt (0.34 wt%).

Table 3. Initial and final concentration, in wt% and mol%, of elements in the synthesized slag analogue, determined by ICP-OES. For the molar fractions, only lithium, silicon, calcium, and manganese are considered.

Mass Fraction/wt%	**Lithium**	**Silicon**	**Calcium**	**Manganese**
expected	2.4	13.0	37.2	9.3
precursor	1.7 ± 0.1	8.9 ± 0.4	26.3 ± 0.7	6.6 ± 0.6
final slag (run A)	2.1 ± 0.1	12.3 ± 0.4	34.9 ± 0.7	9.7 ± 0.6
final slag (run B)	2.0 ± 0.1	12.7 ± 0.4	36.0 ± 0.7	9.3 ± 0.6
Molar Fraction/mol%	**Lithium**	**Silicon**	**Calcium**	**Manganese**
expected	18.0	24.4	48.7	9.0
precursor	18.0 ± 1.5	23.8 ± 1.5	49.2 ± 2.6	9.0 ± 0.9
final slag (run A)	17.0 ± 1.1	24.5 ± 1.2	48.6 ± 1.9	9.8 ± 0.7
final slag (run B)	16.2 ± 1.1	24.9 ± 1.2	49.6 ± 1.9	9.3 ± 0.7

The oxidation state of Mn in the bulk material was obtained using lab-XANES [5]. The Mn K-edge shift of the synthesis precursor matches well with Mn OS: +4 (see the Li_2MnO_3 reference in Figure 2). During the high temperature step, the decomposition of Mn^{4+} to Mn^{3+} takes place, with the XANES spectra resembling the lithium manganate(III) $LiMnO_2$ with small variations due to the possible presence of Mn species with lower oxidation state, e.g., hausmannite Mn_3O_4 or manganese(II) oxide MnO (Figure 2). The change in Mn oxidation state due to high temperatures seen here was also described by Longo et al., Paulsen and Dahn, and Schnickmann et al. [6,7,51].

The diffractograms were obtained from powder samples (laboratory PXRD), as well as from the sum of micro-XRD measurements of a free-standing thin section of the sample. The PXRD of the bulk sample in Figure 3, panel A, indicates the presence of β–Ca_2SiO_4 (larnite). Lithium manganate(III), $LiMnO_2$, and other possible lithium manganates could not be identified unambiguously. Nevertheless, peaks are present in the bulk diffractogram, which are not related to β–Ca_2SiO_4. Due to a high background, based on severe fluorescence, as well as strong overlay because of the high number of peaks given by β–Ca_2SiO_4, these peaks could not yet be assigned to any compound.

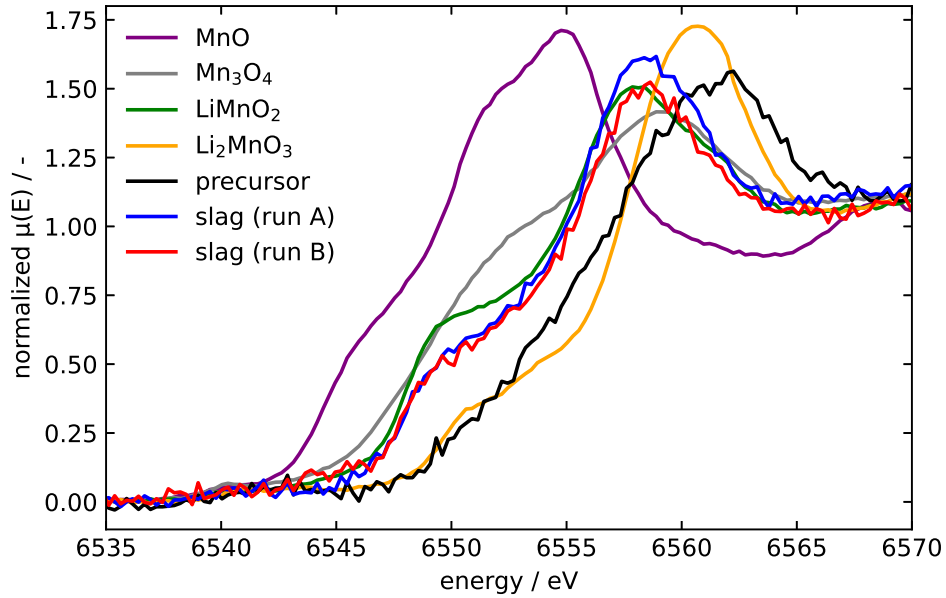

Figure 2. XANES spectra of the Mn K-edge of the slag analogue (precursor and final slags), and the reference compounds MnO, Mn_3O_4, $LiMnO_2$, and Li_2MnO_3.

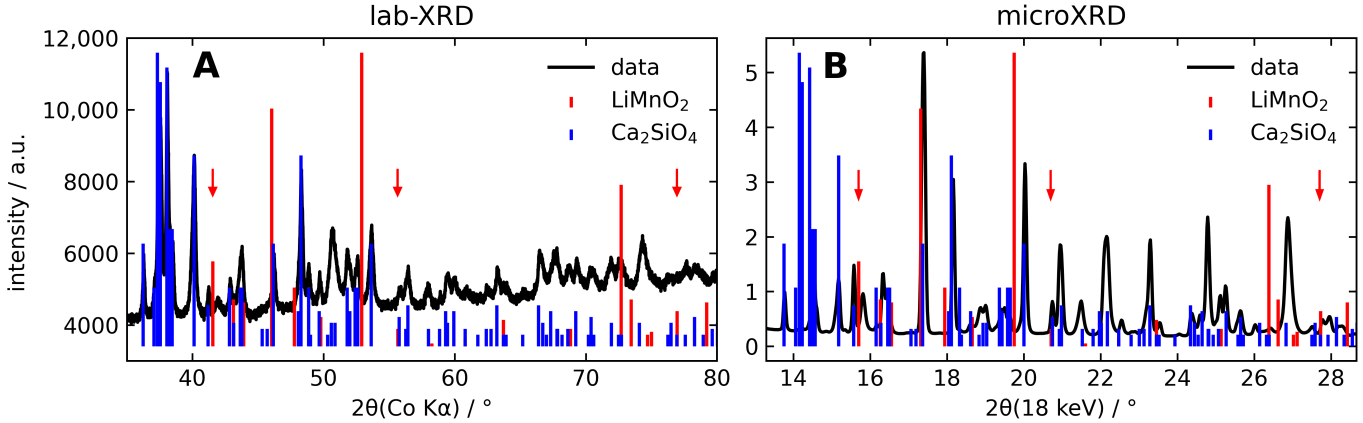

Figure 3. X-ray diffraction data for the quickly cooled melt (run **A**), with indicated references from the PDF-2 database (Ca_2SiO_4 00-009-0351, $LiMnO_2$ 00-035-0749). (**A**) Laboratory powder XRD. (**B**) Summed micro-XRD from a thin section. Note that the micro-XRD diffractogram exhibits lower backgrounds, which makes it easier to identify reflexes. The red arrows indicating the reflexes are possibly associated with the Li-Mn-O compound.

Regarding the sum diffractogram of SR-micro-XRD (see Figure 3B), it has to be mentioned that the sample (free-standing thin film) does not fulfill ideal powder conditions. Therefore, the intensity distribution of the respective reflexes cannot be taken into account, and refinement according to the Rietveld method is not possible. Identification of larnite was performed by Le Bail fit, ignoring intensities and only fitting reflex positions. The model from the refinement of the known phase content (PXRD) does not ideally fit the refinement according to Le Bail. Hence, intensities are present that could not be resolved by prior PXRD. Nevertheless, β–Ca_2SiO_4 can be clearly identified based on the respective reflex positions. Similarly to the PXRD measurement, reflexes that do not belong to β–Ca_2SiO_4 occur, e.g., here at 15.8°, and which might be associated with an Li-Mn-O compound. Three of these reflexes are indicated by red arrows in Figure 3. These reflexes will be discussed further in the micro-XRD section.

The XANES spectra show a predominant presence of Mn OS: +3 species, which resembles $LiMnO_2$. The shoulder suggests the presence of a lithium manganate. The PXRD does not support the presence of crystalline $LiMnO_2$, but shows reflexes not explained by the larnite stemming from a Li-Mn-O compound or compounds.

3.2. Temperature-Dependent Mn Species Evolution from Thermodynamics

Thermodynamic calculations can show the dependence of the Mn oxidation state from the gas phase oxygen concentration and the temperature.

Considering the bulk composition of 5.11 wt% Li_2O, 14.88 wt% MnO_2, 52.09 wt% CaO, and 27.91 wt% SiO_2, the thermodynamic simulations were conducted under equilibrium conditions. In Figure 4A, the release behavior of oxygen from the melt at high temperature is presented at a certain partial pressure of oxygen, 0.21 bar. Additionally, the valence of the manganese in the melt at lower temperatures, where solid phases already appear, is described in Figure 4B. It is shown that the Mn OS: +3 amount decreases and, at the same time, the Mn OS: +2 amount increases by lowering the temperature. At 1673 K, 99.2 mol% of the manganese in the liquid slag is in Mn OS: +3. This indicates that if the slag is cooled down fast from a temperature of 1673 K, manganese is mainly in the Mn OS: +3, and the Mn OS: +2 is suppressed. This is also concluded by the experimental findings, i.e., the XANES discussed before. The model allows us to estimate the influence of temperature and oxygen gas phase concentration on the Mn oxidation state in equilibrium. The effect introduced by oxygen shuttle, as described by Sasabe and Akamura, Nagata and Sasabe [9,52], and non-equilibrium processes can not be described at this time. The microscopic characteristics of the synthesized slag sample are discussed in the following sections. They also show mainly the presence of Mn OS: +3, where Mn OS: +2 was found in very few grains of Mn_3O_4, and with strong evidence in low concentrations in the Ca_2SiO_4 grains.

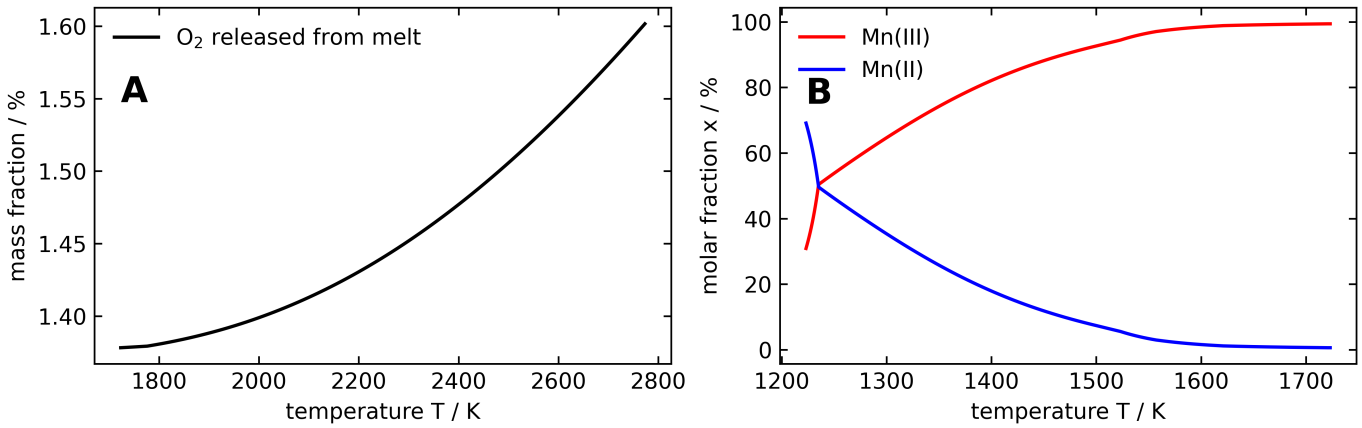

Figure 4. (**A**) Temperature-dependent oxygen release from the melt at $p(O_2)$ = 0.21 bar. (**B**) Temperature-dependent manganese valence of the liquid slag at $p(O_2)$ = 0.21 bar. The red line represents the Mn(III) in the liquid slag, while the blue line shows the Mn(II).

Microscopic Characteristics

The results on the bulk chemistry indicates the presence of larnite and a Li-Mn^{3+}-oxide, with a composition similar to $LiMnO_2$. The microscopic observation of the slag reveals information on the spatial distribution, minor phases, and possibly non-crystalline parts of the sample. The morphology of the grains and their inter-connectivity can be used as basis for a hypothesis of the genesis of the compounds. Using electron probe micro analysis (EPMA) the shape of the grains becomes visible. Here, large grains with smooth roundish curvature have formed; at their rims, either channels of "residual melt" or grains with bright droplets, which seem to have separated from these grains, are present. An example of a back scattering electron image (BSE) is displayed in Figure 5. Phase 1 is located in large round-shaped grains of a uniform gray color, indicating a constant density. The second phase is located in a bright droplet-like feature, where the brighter color indicates a higher

density compared to the other structures. Finally, phase 3 is located in the channels of the residual melt, which is characterized by colors of darker gray, indicating the presence of a lower-density material.

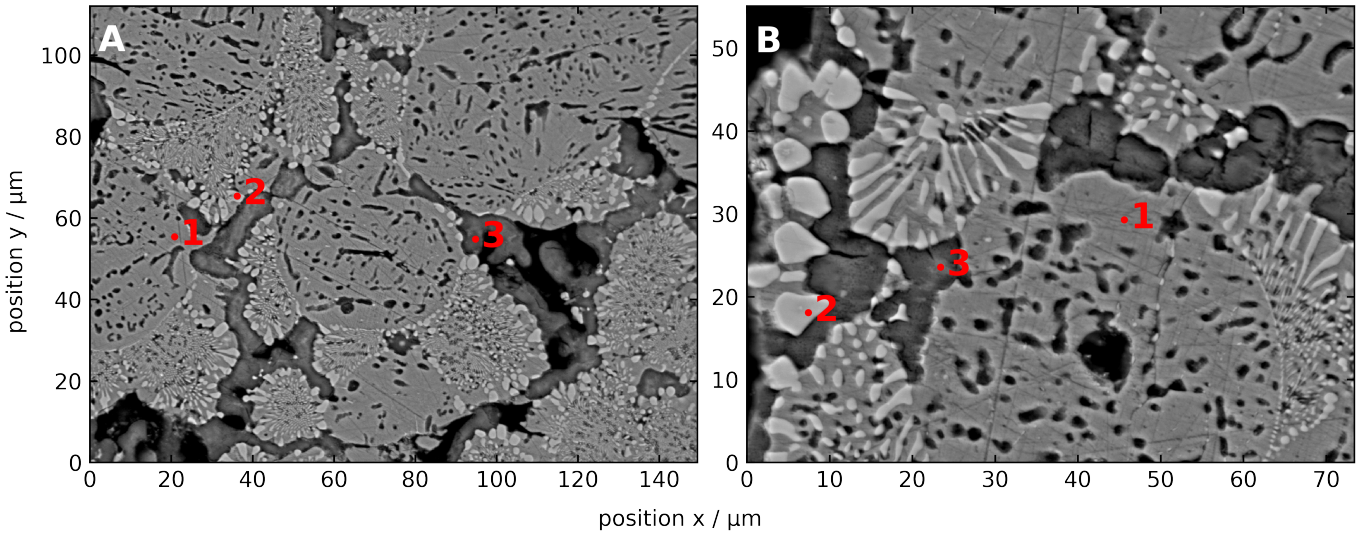

Figure 5. BSE images of the slag analogue from two different regions (**A**) and (**B**). Three characteristic features can be distinguished overall the whole thin section, and are annotated with red numbers 1 to 3 in both regions.

With the characteristic X-ray emission, the composition at the selected spots is determined. Using virtual component fitting, the concentration of oxygen and lithium, which are not available from the experiment, can be concluded [53]. The characteristic morphological features were studied quantitatively by several point measurements. The results for the large grain and the bright droplets are shown in Table 4.

They suggest that the large grains (phase 1 in Figure 5) are largely Ca_2SiO_4, with minor amounts of Mn and the stoichiometric composition of $(Ca_{(2.00)}Mn^{2+}_{(0.02)})_{2.02}(Si_{(0.99)})_{0.99}O_4$ (n = 20). The bright droplets (phase 2 in Figure 5) contain most of the Mn, and the composition is in agreement $LiMnO_2$, with the specific composition $(Li_{(1.86)}Mg_{(0.07)})Mn^{3+}_{2.00}O_4$ (n = 25). The residual melt (phase 3 in Figure 5) has a composition (n = 53) of 6.7 ± 0.7 wt% manganese, 34.6 ± 2.0 wt% calcium, 12.5 ± 0.8 wt% silicon, 0.42 ± 0.25 wt% magnesium, 0.12 ± 0.06 wt% aluminum, and 30.5 ± 1.1 wt% oxygen (total 85.2 ± 2.9 wt%). Magnesium and aluminum may be introduced to the system either by contamination with insulation material of the furnace, or the used crucibles and/or chemicals. However, the concentrations are very low, with <0.21 wt% for Al and <0.63 wt% Mg. The influence of both elements in concentrations of about 1.1–1.2 wt% was probed in a previous study [6]. There, it was shown that Mg leads to a less diverse occurrence of compounds, while Al and Mg results in a number of solid solutions. The virtual component fitting of the calcium-silicate phase predicts that Mn is present in the OS: +2 as a silicate. The elemental maps, also obtained with the EPMA, show that Ca and Si are correlated, while Mn is mainly anti-correlated with Ca and Si in agreement with the point measurements. The back-scatter images, as well as the elemental maps of Mg, Mn, Ca and Si for two regions, are displayed in Figure 6. The BSE image (Figure 5B) is shown in the top row, while for the bottom row, a new region was chosen to confirm the findings.

Table 4. Mean mass fractions of marked phases in Figure 5 with EPMA (WDXRF) and virtual components.

	Phase 1: $(Ca_{(2.00)}Mn^{2+}_{(0.02)})_{2.02}(Si_{(0.99)})_{0.99}O_4$			Phase 2: $(Li_{(1.86)}Mg_{(0.07)})Mn^{3+}_{2.00}O_4$		
Mass Fraction/wt%	**Ca_2SiO_4**	**Mn_2SiO_4**	**Total**	**$LiMnO_2$**	**$MgMn_2O_4$**	**Total**
Li	–	–	–	6.83	–	6.83
Mn(II)	–	0.64	0.64	–	–	–
Mn(III)	–	–	–	54.03	4.13	58.16
Si	15.62	0.16	15.78	–	–	–
Ca	45.70	–	45.70	–	–	–
Mg	–	–	–	–	0.91	0.91
O	36.03	0.37	36.41	31.47	2.40	33.88
sum	97.35	1.17	98.52	92.33	7.45	99.78

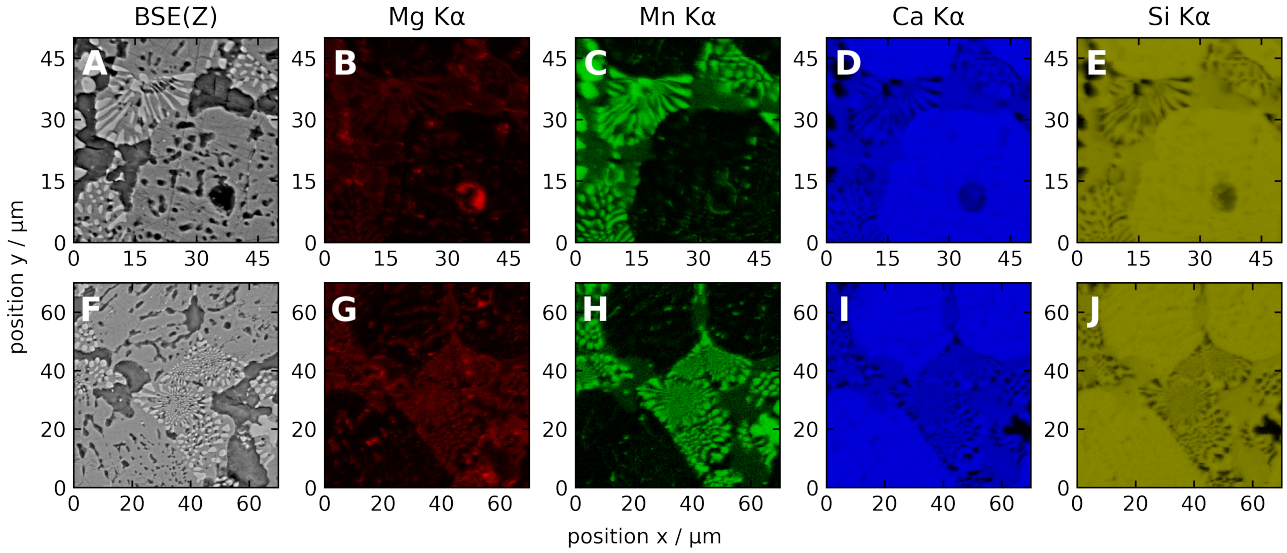

Figure 6. Mapping results obtained from EPMA exemplary from two regions of the specimen (**top** and **bottom**); (**A**,**F**): BSE images, false color images: Mg Kα (**B**,**G**, red), Mn Kα (**C**,**H**, green), Ca Kα (**D**,**I**, blue), and Si Kα (**E**,**J**, yellow).

The Mn oxidation states in the $LiMnO_2$ and the Ca_2SiO_4 predicted by the virtual component fitting was studied by species analysis using micro-XANES, with slightly lower spatial resolution at the Diamond Light Source at end station I18. A large area of the specimen was analyzed by micro-XRF to identify the grains, followed by energy scans to determine the Mn K-edge absorption edge fine structure at every pixel. The structure of the edges were compared with spectra obtained from Mn reference compounds. The XANES of manganese oxides spanning oxidation states from +2 to +4 ($Mn^{2+}O$, $Mn_2{}^{3+}O_3$, $Mn_3{}^{2.67+}O_4$ and $Mn^{4+}O_2$), including lithium manganates ($LiMn_2{}^{3.5+}O_4$, $Li_2Mn^{4+}O_3$, $LiMn^{3+}O_2$), are displayed in Figure 7A,B. As expected, the energy of the main edge shifts with higher oxidation state to higher energies. Additionally, the lithium-bearing compounds show a low energy shoulder as a common characteristic. The references were used in linear combination fittings to identify the Mn species in each pixel. Three different (mostly spatially separated) Mn species were identified. These are a Li-Mn^{3+}-oxide, $Mn_3{}^{2.67+}O_4$, and an unidentified species. The main Mn species shows the shoulder characteristic for lithium manganates, and a main edge shift characteristic for Mn OS: +3. The $Mn_3{}^{2.67+}O_4$ seems to be associated with the Li-Mn^{3+}-oxide, and the unidentified species is present in the Ca_2SiO_4. The XANES of the three regions is shown in Figure 7C.

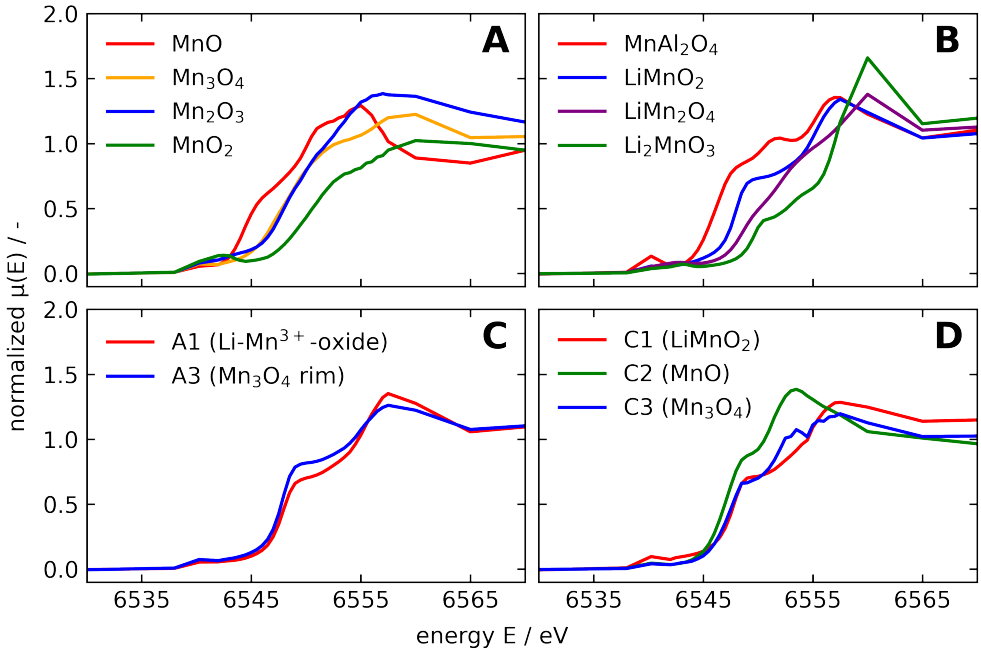

Figure 7. Manganese K-edge XANES spectra of manganese specimens. (**A**): manganese oxides references. (**B**): lithium manganese oxides and manganese aluminum oxide references. (**C**): two species identified in the fast-cooled slag specimen with ROI 1 Li-Mn^{3+}-oxide and ROI 3 $Mn_3^{2.67+}O_4$ rim. (**D**): three species identified in the slowly cooled slag specimen with ROI 1 Li-Mn^{3+}-oxide, ROI 2 Mn^{2+} species and ROI 3 $Mn_3^{2.67+}O_4$.

The speciation of Mn in the Ca_2SiO_4 is not possible, due to (a) overlapping with the Li-Mn^{3+}-oxide spectra from greater depths (the free-standing thin film is polished to about 50 µm thickness, and only small grains of the Li-Mn-O compounds in depth will dominate the XANES), (b) lower concentrations expressed as edge-jump (up to 10 times lower than in the red areas), and (c) resulting errors in the linear combination fit (LCF) expressed as R factor. The R factor describes the goodness-of-fit with perfect results at R = 0 and rising with increasing errors [54]. The same applies for the Mn_3O_4 rim, while here, better statistics and changes in the edge region towards the reference spectrum allow a correct assignment. The micro-XANES LCF high fit errors correlate with low concentrations (e.g., in the Ca_2SiO_4 grains). The correlation is visualized in Figure S1 in the Supplementary Materials.

In Figure 8, an overview of the elemental distribution is shown as an RGB image in part A, with Ca (blue), Mn (red) and Pt < 0.34 wt% (green). The low concentrated contamination of Pt stemming from the crucibles is included, as it is enriched in the residual melt. The species distribution is displayed from a close-up, which is indicated as a white box. The elemental distribution of the close-up area is shown in Figure 8B, and the assigned Mn species in part C. The Mn species obtained from the micro-XANES data are Li-Mn^{3+}-oxide (red), Mn species unknown (green), and $Mn_3^{2.67+}O_4$ (blue).

The bulk PXRD was inconclusive on the presence of $LiMnO_2$. The EPMA with virtual components and the micro-XANES indicate the presence of a compound/compounds with a composition similar to $LiMnO_2$. In Figure 3, the summed diffractogram of micro-XRD measurements showed reflexes that do not belong to β–Ca_2SiO_4 (2θ(18 keV) = 15.8°, 20.6°, and 27.5°), and which could possibly belong to a Li-Mn-O structure. Processing of the micro-XRD data allows us to test for spatial correlation of these reflexes with the Mn-rich grains. The intensity map for the reflex 15.8° 2θ is shown in Figure 9 (the reflex 15.8° 2θ matched this position, while the 27.5° reflex showed the same map with lower intensity). In panel A, the intensity map for the reflex shown resembles a structure around the large grains. In panel B, the micro-XRF data for Ca and Mn are shown, exhibiting no clear correlation with the above mentioned intensity map (Figure 9A). Figure 9C, on the other hand, shows transmission data, capturing the grain structure in depth. The transmission

data and micro-XRD data were obtained through the entire thin section, giving evidence that several grains were present within the thickness of the thin section. The overlay with the reflex data of $2\theta = 15.8°$ show that it represents a structure surrounding larnite grains. The "droplet spray" structure visible in the EPMA incorporates most of the Mn present in the sample (Figure 9B); therefore, the intensities plotted in panel C indicate the presence of an Li-Mn-O structure around the larnite grains. The exact structure of this Li-Mn-O compound cannot be identified unambiguously, which is basically given by the severe overlay with larnite intensities. The EPMA images show that the Li-Mn-O grains are mostly quite small, with 2–5 µm; the isolation of $LiMnO_2$ from larnite reflexes with an resolution of 2 µm, in combination with the several grain layers in the 50 µm thick specimen, was not possible. Regarding the calculated stoichiometry of the Li-Mn-O compound, $LiMnO_2$ would be a promising candidate; additionally, the (011) peak of $LiMnO_2$ fits to the certain 2θ position shown in Figure 9A. Nevertheless, prior PXRD measurements could not confirm the presence of the structure of $LiMnO_2$. Therefore, $LiMnO_2$ is either present in the sample in very small quantities, which can only be visualized by micro-XRD analysis, or the observed intensities belong to another structurally different Li-Mn-O compound.

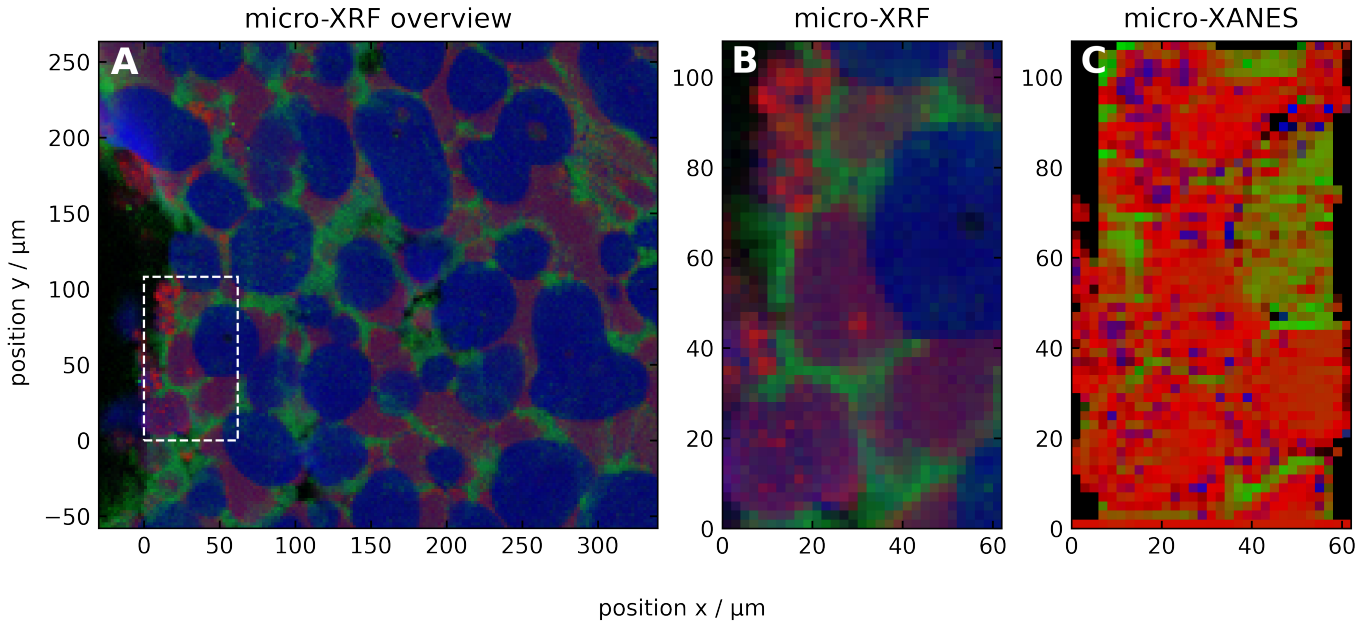

Figure 8. RGB false color image of the fast-cooled slag analogue. (**A**) Overview with the selected area indicated; (**B**) close-up of the elemental distribution of Ca (blue), Mn (red) and Pt < 0.34 wt% (green); (**C**) distribution of the Mn species obtained from the micro-XANES data: Li-Mn^{3+}-oxide (red), Mn species unknown (green), and $Mn_3{}^{2.67+}O_4$ (blue).

In conclusion, the Mn oxidation state in the Mn-rich grains, determined from the micro-XANES, is +3, and matches the results from the EPMA well. The $Mn_3{}^{2.67+}O_4$ phase was not identified initially with the EPMA, but with the micro-XANES. The Mn oxidation state in the larnite could not be determined. In a slowly cooled slag with similar composition, which has been described previously [6], $LiMnO_2$ and larnite were identified. The larnite also contained low amounts of Mn. Here, the slowly cooled slag was also subjected to micro-XANES, to confirm the Mn species and attempt the speciation of Mn in the larnite. The Mn OS: +3 was confirmed in the Mn-rich needles and, like in the fast cooled counterpart, hausmannite was identified in adjacent areas. Due to the better statistic of the measurements, it was possible to identify the Mn species, being +2. Deeper insights on the chemical composition of the compound were not obtained. The XANES spectra of the reference oxides were not matching. In future studies, manganese silicates (e.g., tephroite Mn_2SiO_4) could be an interesting reference. In Figure 7, the Mn K-edge XANES spectra for the three identified species are displayed. These are $LiMn^{3+}O_2$ (ROI 1 red), $Mn_3{}^{2.67+}O_4$

(ROI 3 blue), and the Mn +2 (ROI 2 green). The distribution of elements and Mn species are shown in Figure 10. In A, an RGB false color image of the elemental distribution is shown, with the Ca matrix in blue, Mn in red, and Pt in green (Pt is present in very low concentrations from the crucible). In part C, the Mn species distribution is shown. The Mn-rich needle-like grains match with $LiMn^{3+}O_2$ (red). At the rims of the needle, the spectra match $Mn_3^{2.67+}O_4$ (blue), and in the calcium matrix, the Mn+2 species is present (green).

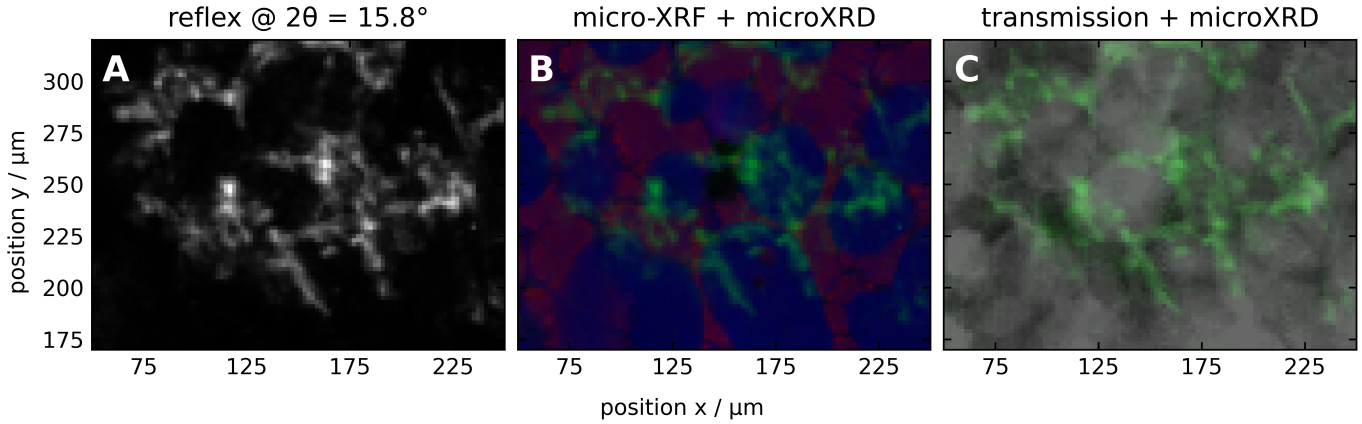

Figure 9. (**A**): micro-XRD intensity map of possible $LiMnO_2$ (011) reflex at 15.8° 2θ. (**B**): RGB false color image of micro-XRD map of 15.8° reflex (green), and micro-XRF elemental distribution of Ca (blue) and Mn (red). (**C**): false color image of micro-XRD map of 15.8° reflex (green) and transmission signal (gray scale).

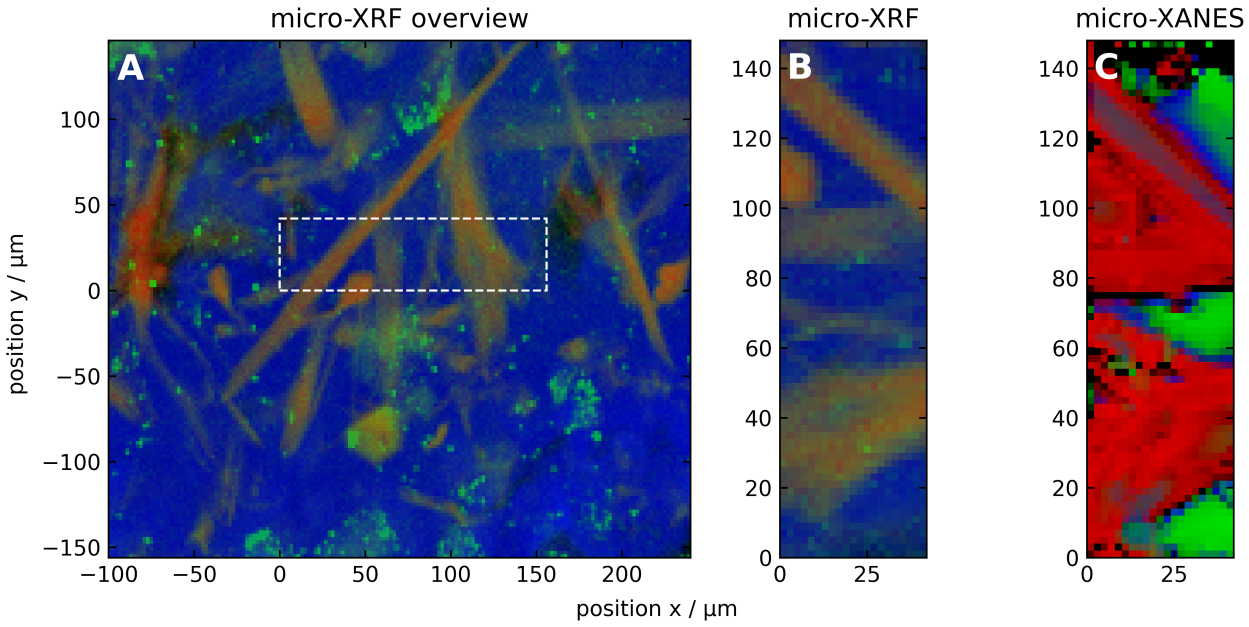

Figure 10. RGB false color image of the slowly cooled slag analogue. (**A**) Overview with the selected area indicated; (**B**) close-up of the elemental distribution of Ca (blue), Mn (red) and Pt < 0.34 wt% (green); (**C**) distribution of the Mn species obtained from the micro-XANES data: $LiMn^{3+}O_2$ (red), Mn +2 species (green) and $Mn_3^{2.67+}O_4$ (blue).

3.3. Modeling of Mn Species Evolution and of Potential Melt Structures

A central question in the genesis of compounds in the slag is which parameters govern the oxidation state of redox-active species, here manganese. We have shown that Mn of OS: +3 is the main species in the slags studied here, and there is strong evidence that Mn of OS: +2 is present in the calcium silicate phase. The oxidizing agent responsible for higher

valence is most likely oxygen, which needs to be transferred between the gas phase and the melt. Parameters influencing the oxygen transfer are its concentration in the gas phase, the temperature-dependent equilibrium, the viscosity of the melt [2,8], and the concentration of labile redox active metal ions in the melt [9]. In general, a lower viscosity favors a higher permeability of oxygen [1,2,8]. The viscosity of different composited slags can be estimated by considering network breaking, i.e., Fe and Mn ions, and network-forming ions, e.g., Si, as well as calculating the degree of polymerization Q [1,2]. However, the local viscosity will be influenced by phase separation, and is usually not addressed in these models. Liquid–liquid separation, as well as liquid–solid separation, can commonly occur in silicate-based melts. If a immiscibility gap is thermodynamically present, it manifests itself at low viscosities. Permeation of gas phase oxygen has been intensively studied with respect to redox-active oxides like Fe and Mn, and it was found that increasing the concentration of these significantly increases oxygen permeability because of a redox-mediated dissolution of oxygen [9,52]. As these ions also act as network breakers both effects, lowering of the viscosity and facilitating the redox-mediated oxygen transport occur together with the presence of manganese ions.

Potential Local Melt Structures and Viscosity by MD Simulations

Assuming the phases $LiMn^{3+}O_2$ and Ca_2SiO_4 were present in micro-areas of the melt, those were chosen to simulate their MD at high temperatures. Starting from below the liquidus to above the liquidus, the MD simulations allow us to obtain information over this temperature range by applying the potentials discussed in experimental section. However, the elemental composition in the simulated cube is fixed, and decompositions are not included at this point.

The mean square displacement function of the ions at different temperatures, and the diffusion coefficients of the individual ions in the two phases, are calculated. It was previously shown that Li^+ ions are most mobile [24]; this was found here as well, in the lithium manganate phase with, e.g., diffusion coefficients of 0.45×10^{-9} $m^2 \cdot s^{-1}$ at 1700 K and 20.28×10^{-9} $m^2 \cdot s^{-1}$ at 2100 K. The manganese cations and the oxygen anions have quite similar diffusion coefficients, with 0.7×10^{-11} $m^2 \cdot s^{-1}$ for Mn^{3+} and 0.3×10^{-11} $m^2 \cdot s^{-1}$ for O^{2-} at 1700 K, as well as 3.77×10^{-9} $m^2 \cdot s^{-1}$ for Mn^{3+} and 4.99×10^{-9} $m^2 \cdot s^{-1}$ for O^{2-} at 2100 K (Figure 11, left). In the calcium silicate phase, the mobility of the ions is significantly lower. The Ca^{2+} ions are most mobile (however, much less compared to lithium ions) in this phase, and reach a diffusion coefficient of 5.94×10^{-9} $m^2 \cdot s^{-1}$ at 2400 K. The silicon and oxygen ions have similar mobility, lower than the one of the calcium ions of 2.26×10^{-9} $m^2 \cdot s^{-1}$ Si^{4+} and 2.77×10^{-9} $m^2 \cdot s^{-1}$ O^{2-} at 2400 K (Figure 11, right).

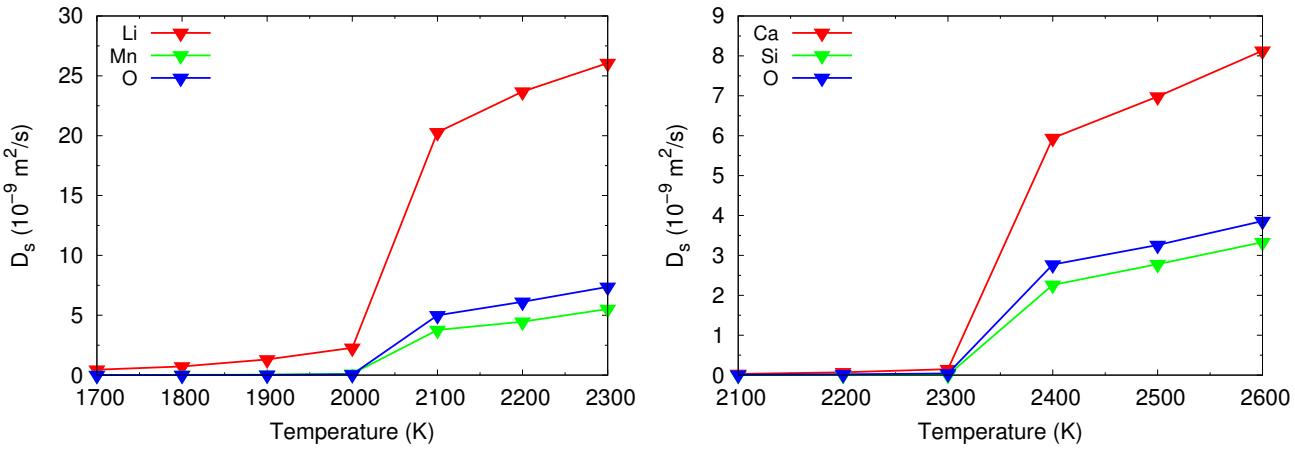

Figure 11. Temperature-dependent diffusion coefficient for the different ions. Left: Li^+ (red), Mn^{3+} (green), and O^{2-} (blue). Right: Ca^{2+} (red), Si^{4+} (green), and O^{2-} (blue).

The mean coordination number of ions can be computed by counting the number of neighbors of an ion within a given cutoff distance and averaged over the ions of the same species. It is found that each Si ion that moves in the slag is surrounded by four oxygen ions. The coordination numbers for Si-Si interactions are a good indicator for the degree of polymerization. The average coordination number given from the distribution in Figure 12 is 1.05, showing only small polymerization degree for Si-Si interaction. For Si-O interactions, the mean coordination number is close to 4, representing the formation of the SiO_4 tetrahedra shown in Figure 12 (right side).

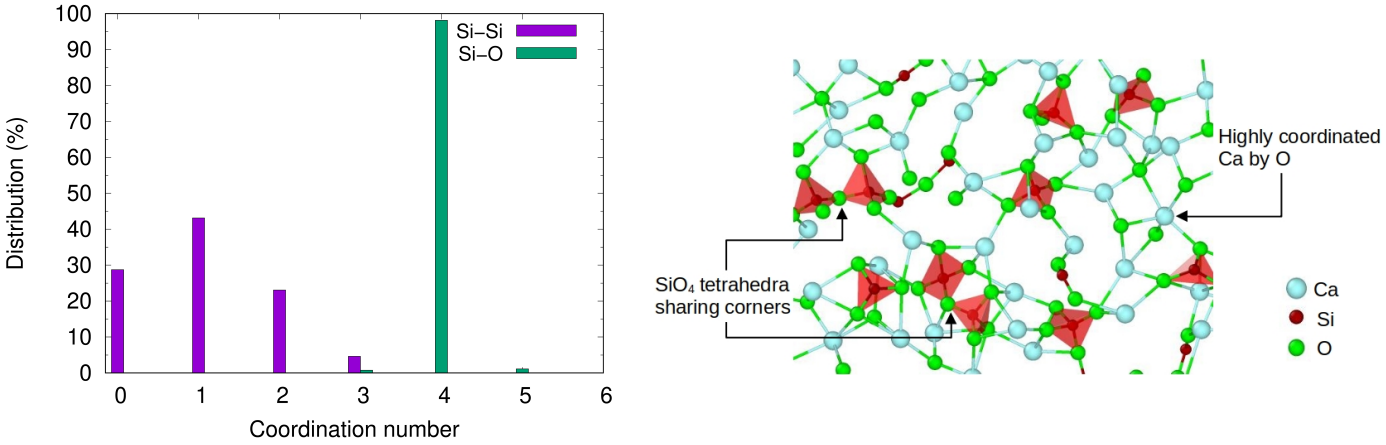

Figure 12. Distribution of coordination numbers of Si-Si and Si-O interactions (**left**). Graphic representation of the Ca_2SiO_4 slag structure (**right**).

The affinity for Si-O bonds can be best shown from the radial distribution function (RDF) at melt conditions (see Figure S2, Supplementary Materials). Figure S2 visualizes the RDF for $LiMnO_2$ and Ca_2SiO_4 at 2100 K and 2400 K, respectively. For Ca_2SiO_4, the strong Si-O bonds are well visible, with Ca being incorporated into the SiO_x network. For the Li-Mn-O interactions in $LiMnO_2$, comparable bond lengths for Li-O and Mn-O were obtained. Consequently, the viscosity of the calcium silicate phase is significantly higher compared to the lithium manganate phase. Viscosity depends on composition and temperature, as can be seen in Figure 13. At 1800 K, a temperature close to the melt temperature during slag preparation (1673 K), the viscosity of the $LiMn^{3+}O_2$ is 50.51 mPa·s, while the viscosity of the Ca_2SiO_4 is higher > 634.74 mPa·s.

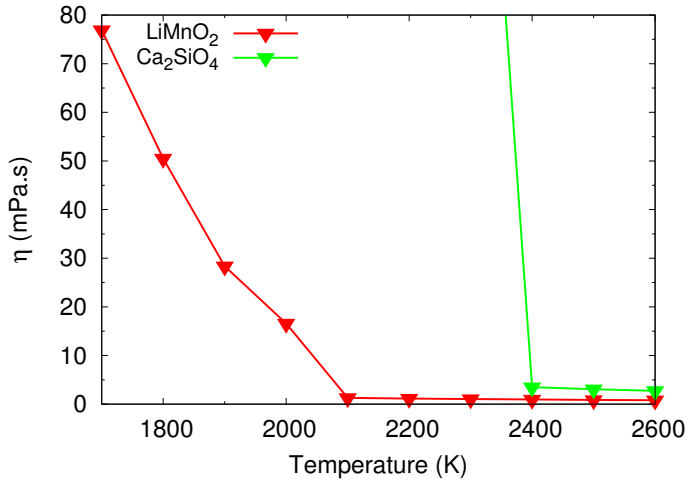

Figure 13. Temperature-dependent viscosity of $LiMn^{3+}O_2$ (red) and Ca_2SiO_4 (green).

The elemental analysis (cf. to Section 3.1) and the EPMA has shown that the phases are not pure. The calcium silicate contains approx. 0.7 wt% Mn, and the lithium manganate(III) phase

contains 0.9 wt% magnesium. Accordingly, it is expected that the actual viscosity of the phases are lower than those simulated. The contamination will be included in future simulations.

4. Conclusions

Pyrometallurgical Li-ion battery slags are rich in Li, and also contain a fair amount of Mn. The oxidation state of the Mn can vary from elemental to +4 and, accordingly, different compounds are formed. The ability to produce specific compounds in the slag can be favorable when using it as a secondary resource for critical elements. The conditions for an efficient recycling of Li from these slags are mainly that the Li is concentrated in a single compound, which can be easily separated from the rest. Therefore, it is important to understand what governs the Mn oxidation state evolution. Here, the formation of the Mn oxidation state in a calcium silicate system containing approx. 17 wt% lithium manganate(III) was studied. The solidified product, which has encountered steep cooling rates, showed separation into round large larnite grains and small Li-Mn-Oxide droplets close to each other (spray-like pattern). Mainly Mn OS: +3 was formed in the Li-Mn-rich grains, with evidence of the chemical composition being $LiMnO_2$. Manganese OS: +2 was found in small concentrations in the calcium silicate phase and in the hausmannite phase. Thermodynamic simulations under the assumption that the melt is homogeneous predict a dominance of Mn^{3+} over Mn^{2+}, with a fraction of 99 mol% at experimental temperature of 1673 K. The fast cooling may have preserved this status. The viscosity of a Ca_2SiO_4 and $LiMnO_2$ as potential micro compositions of the melt at 1700 K obtained with MD simulation showed significant differences. The viscosity of the $LiMnO_2$ phase was, indeed, lower than the one of the Ca_2SiO_4, which could suggest that lower viscosity will support higher Mn oxidation state, at least up to a certain temperature. With a proper understanding of the influence of viscosity and composition on Mn species, the design of scavenging compounds directly in the slag comes into reach. This can facilitate the efficient recovery of elements like Li from already-established recycling processes like pyrometallurgical recycling of Li-ion batteries.

Supplementary Materials: The following supporting information can be downloaded at: https://www.mdpi.com/article/10.3390/min14090868/s1, Figure S1: R factors and edge jumps from micro-XANES and micro-XANES linear combination fit; Figure S2: Radial distribution function for the different ions in $LiMnO_2$ (at 2100 K) and Ca_2SiO_4 (at 2400 K).

Author Contributions: Conceptualization, U.E.A.F.; investigation, S.H., I.A.A., A.S., S.W. and H.L.; writing—original draft preparation, S.H., I.A.A. and U.E.A.F.; writing—review and editing, A.S., S.W., H.L., M.F., T.S. and N.M.; visualization, S.H. and I.A.A.; supervision, M.F., T.S., N.M. and U.E.A.F.; project administration, U.E.A.F.; funding acquisition, M.F., T.S., N.M. and U.E.A.F. All authors have read and agreed to the published version of the manuscript.

Funding: This research was funded by the German Research Foundation as part of the priority program: Engineered Artificial Minerals (EnAM)—a geometallurgical tool for the recovery of critical elements from waste streams (SPP 2315, ProjNo. 470367641, 470309740, and 470323858). Further funding was granted by the German Research Foundation under the ProjNo 426693405.

Data Availability Statement: Data are contained within the article and supplementary materials.

Acknowledgments: We acknowledge Diamond Light Source for time on beamline I18 under proposal 32108. The authors thank Sylvia Britto (I18, Diamond Light Source) for the local support during the beamtime. We further thank Karin Bode (Clausthal University of Technology, Institute of Inorganic and Analytical Chemistry) for elemental analysis (CHNS) as well as Petra Lassen (Clausthal University of Technology, Institute of Inorganic and Analytical Chemistry) and Heike Grosse (Clausthal University of Technology, Institute of Mineral and Waste Processing, Recycling and Circular Economy Systems) for ICP-OES measurements. The Institute of Mineral and Waste Processing, Recycling and Circular Economy Systems is also acknowledged for the provision of high temperature furnace for slag preparation. We acknowledge the support by Open Access Publishing Fund of Clausthal University of Technology.

Conflicts of Interest: The authors declare no conflicts of interest. The funders had no role in the design of the study, in the collection, analyses, or interpretation of data, in the writing of the manuscript, or in the decision to publish the results. Sophie Wunderlich was employed by the company Salzgitter Mannesmann Forschung. The remaining authors declare that the research was conducted in the absence of any commercial or financial relationships that could be construed as a potential conflict of interest.

References

1. Mills, K.C. The Influence of Structure on the Physico-chemical Properties of Slags. *ISIJ Int.* **1993**, *33*, 148–155. [CrossRef]
2. Mills, K.C.; Hayashi, M.; Wang, L.; Watanabe, T. Chapter 2.2—The Structure and Properties of Silicate Slags. In *Treatise on Process Metallurgy*; Seetharaman, S., Ed.; Elsevier: Boston, MA, USA, 2014; pp. 149–286. [CrossRef]
3. Elwert, T.; Strauss, K.; Schirmer, T.; Goldmann, D. Phase composition of high lithium slags from the recycling of lithium ion batteries. *World Metall.-Erzmetall* **2012**, *65*, 163–171.
4. Acker, S.; Namyslo, J.C.; Rudolph, M.; Strube, F.; Fittschen, U.E.A.; Qiu, H.; Goldmann, D.; Schmidt, A. Polyether-tethered imidazole-2-thiones, imidazole-2-selenones and imidazolium salts as collectors for the flotation of lithium aluminate and spodumene. *RSC Adv.* **2023**, *13*, 6593–6605. [CrossRef] [PubMed]
5. Wittkowski, A.; Schirmer, T.; Qiu, H.; Goldmann, D.; Fittschen, U.E.A. Speciation of Manganese in a Synthetic Recycling Slag Relevant for Lithium Recycling from Lithium-Ion Batteries. *Metals* **2021**, *11*, 188. [CrossRef]
6. Schnickmann, A.; Hampel, S.; Schirmer, T.; Fittschen, U.E.A. Formation of Lithium-Manganates in a Complex Slag System Consisting of Li_2O-MgO-Al_2O_3-SiO_2-CaO-MnO—A First Survey. *Metals* **2023**, *13*, 2006. [CrossRef]
7. Longo, R.C.; Kong, F.T.; KC, S.; Park, M.S.; Yoon, J.; Yeon, D.H.; Park, J.H.; Doo, S.G.; Cho, K. Phase stability of Li–Mn–O oxides as cathode materials for Li-ion batteries: Insights from ab initio calculations. *Phys. Chem. Chem. Phys.* **2014**, *16*, 11233–11242. [CrossRef] [PubMed]
8. Jahanshahi, S.; Sun, S.; Zhang, L. Effects of transition metals on physicochemical properties of slags. In Proceedings of the International Conference on Advanced Metallurgical Processes and Materials, Dnipropetrovsk, Ukraine, 27–30 May 2007; pp. 1–20.
9. Nagata, K.; Sasabe, M. Permeability Coefficient of Oxygen in Molten Slags and Its Mechanisms. *ISIJ Int.* **2020**, *60*, 1872–1877. [CrossRef]
10. Lukas, H.; Fries, S.G.; Sundman, B. *Computational Thermodynamics: The Calphad Method*; Cambridge University Press: Cambridge, UK, 2007. [CrossRef]
11. Li, H.; Qiu, H.; Schirmer, T.; Goldmann, D.; Fischlschweiger, M. Tailoring Lithium Aluminate Phases Based on Thermodynamics for an Increased Recycling Efficiency of Li-Ion Batteries. *ACS ES&T Eng.* **2022**, *2*, 1883–1895. [CrossRef]
12. Li, H.; Ranneberg, M.; Fischlschweiger, M. High-Temperature Phase Behavior of Li_2O-MnO with a Focus on the Liquid-to-Solid Transition. *JOM* **2023**, *75*, 5796–5807. [CrossRef]
13. Bale, C.; Bélisle, E.; Chartrand, P.; Decterov, S.; Eriksson, G.; Gheribi, A.; Hack, K.; Jung, I.H.; Kang, Y.B.; Melançon, J.; et al. FactSage thermochemical software and databases, 2010–2016. *Calphad* **2016**, *54*, 35–53. [CrossRef]
14. Chakrabarty, S.; Li, H.; Fischlschweiger, M. Calphad-informed thermodynamic non-equilibrium simulation of non-isothermal solid-state reactions of magnesium aluminate spinel based on the thermodynamic extremal principle. *Materialia* **2023**, *28*, 101723. [CrossRef]
15. Schirmer, T.; Qiu, H.; Li, H.; Goldmann, D.; Fischlschweiger, M. Li-Distribution in Compounds of the Li_2O-MgO-Al_2O_3-SiO_2-CaO System—A First Survey. *Metals* **2020**, *10*, 1633. [CrossRef]
16. Sommerfeld, M.; Vonderstein, C.; Dertmann, C.; Klimko, J.; Oráč, D.; Miškufová, A.; Havlík, T.; Friedrich, B. A Combined Pyro- and Hydrometallurgical Approach to Recycle Pyrolyzed Lithium-Ion Battery Black Mass Part 1: Production of Lithium Concentrates in an Electric Arc Furnace. *Metals* **2020**, *10*, 1069. [CrossRef]
17. Zhou, C.; Li, J.; Wang, S.; Zhao, J.; Ai, L.; Chen, Q.; Chen, Q.; Zhao, D. Development of Molecular Dynamics and Research Progress in the Study of Slag. *Materials* **2023**, *16*, 5373. [CrossRef]
18. Kim, Y.; Park, H. Estimation of TiO_2-FeO-Na_2O slag viscosity through molecular dynamics simulations for an energy efficient ilmenite smelting process. *Sci. Rep.* **2019**, *9*, 17338. [CrossRef]
19. Ma, S.; Li, K.; Zhang, J.; Jiang, C.; Bi, Z.; Sun, M.; Wang, Z. Effect of MnO content on slag structure and properties under different basicity conditions: A molecular dynamics study. *J. Mol. Liq.* **2021**, *336*, 116304. [CrossRef]
20. Liang, D.; Yan, Z.; Lv, X.; Zhang, J.; Bai, C. Transition of Blast Furnace Slag from Silicate-Based to Aluminate-Based: Structure Evolution by Molecular Dynamics Simulation and Raman Spectroscopy. *Metall. Mater. Trans. B* **2017**, *48*, 573–581. [CrossRef]
21. Zhang, X.; Liu, C.; Jiang, M. Molecular Dynamics Simulations of Melt Structure Properties of CaO–Al_2O_3–Na_2O Slag. *Metall. Mater. Trans. B* **2021**, *52*, 2604–2611. [CrossRef]
22. Deng, L.; Zhang, X.; Zhang, M.; Jia, X. Effect of CaF_2 on viscosity, structure and properties of CaO-Al_2O_3-MgO-SiO_2 slag glass ceramics. *J. Non-Cryst. Solids* **2018**, *500*, 310–316. [CrossRef]
23. Chen, Y.; Pan, W.; Jia, B.; Wang, Q.; Zhang, X.; Wang, Q.; He, S. Effects of the amphoteric behavior of Al_2O_3 on the structure and properties of CaO–SiO_2–Al_2O_3 melts by molecular dynamics. *J. Non-Cryst. Solids* **2021**, *552*, 120435. [CrossRef]

24. Hampel, S.; Alhafez, I.A.; Schirmer, T.; Merkert, N.; Wunderlich, S.; Schnickmann, A.; Li, H.; Fischlschweiger, M.; Fittschen, U.E.A. Engineering Compounds for the Recovery of Critical Elements from Slags: Melt Characteristics of Li_5AlO_4, $LiAlO_2$, and $LiAl_5O_8$. *ACS Omega* **2024**, *9*, 24584–24592. [CrossRef] [PubMed]
25. Fittschen, U.E.; Hampel, S.; Schirmer, T.; Merkert, N. Multimodal spectroscopy and Molecular Dynamic simulations to understand redox-chemistry and compound formation in pyrometallurgical slags: Example of manganese oxidation state with respect to lithium recycling. *Appl. Spectrosc. Rev. Laps* **2024**, *59*, 780–797. [CrossRef]
26. Thompson, A.P.; Aktulga, H.M.; Berger, R.; Bolintineanu, D.S.; Brown, W.M.; Crozier, P.S.; in 't Veld, P.J.; Kohlmeyer, A.; Moore, S.G.; Nguyen, T.D.; et al. LAMMPS—A flexible simulation tool for particle-based materials modeling at the atomic, meso, and continuum scales. *Comput. Phys. Commun.* **2022**, *271*, 108171. [CrossRef]
27. Cormack, A.; Du, J. Molecular dynamics simulations of soda–lime–silicate glasses. *J. Non-Cryst. Solids* **2001**, *293–295*, 283–289. [CrossRef]
28. Sayle, T.X.T.; Ngoepe, P.E.; Sayle, D.C. Simulating Mechanical Deformation in Nanomaterials with Application for Energy Storage in Nanoporous Architectures. *ACS Nano* **2009**, *3*, 3308–3314. [CrossRef] [PubMed]
29. Jain, A.; Ong, S.P.; Hautier, G.; Chen, W.; Richards, W.D.; Dacek, S.; Cholia, S.; Gunter, D.; Skinner, D.; Ceder, G.; et al. Commentary: The Materials Project: A materials genome approach to accelerating materials innovation. *APL Mater.* **2013**, *1*, 011002. [CrossRef]
30. Stukowski, A. Visualization and analysis of atomistic simulation data with OVITO-the Open Visualization Tool. *Model. Simul. Mater. Sci. Eng.* **2010**, *18*, 015012. [CrossRef]
31. Pelton, A.D.; Degterov, S.A.; Eriksson, G.; Robelin, C.; Dessureault, Y. The modified quasichemical model I—Binary solutions. *Metall. Mater. Trans. B* **2000**, *31*, 651–659. [CrossRef]
32. Pelton, A.D.; Chartrand, P. The modified quasi-chemical model: Part II. Multicomponent solutions. *Metall. Mater. Trans. A* **2001**, *32*, 1355–1360. [CrossRef]
33. Pelton, A.D. A general "geometric" thermodynamic model for multicomponent solutions. *Calphad* **2001**, *25*, 319–328. [CrossRef]
34. Seidler, G.T.; Mortensen, D.R.; Remesnik, A.J.; Pacold, J.I.; Ball, N.A.; Barry, N.; Styczinski, M.; Hoidn, O.R. A laboratory-based hard X-ray monochromator for high-resolution X-ray emission spectroscopy and X-ray absorption near edge structure measurements. *Rev. Sci. Instrum.* **2014**, *85*, 113906. [CrossRef]
35. Jahrman, E.P.; Holden, W.M.; Ditter, A.S.; Mortensen, D.R.; Seidler, G.T.; Fister, T.T.; Kozimor, S.A.; Piper, L.F.J.; Rana, J.; Hyatt, N.C.; et al. An improved laboratory-based X-ray absorption fine structure and X-ray emission spectrometer for analytical applications in materials chemistry research. *Rev. Sci. Instrum.* **2019**, *90*, 024106. [CrossRef] [PubMed]
36. Ravel, B.; Newville, M. ATHENA, ARTEMIS, HEPHAESTUS: Data analysis for X-ray absorption spectroscopy using IFEFFIT. *J. Synchrotron Radiat.* **2005**, *12*, 537–541. [CrossRef] [PubMed]
37. Gates-Rector, S.; Blanton, T. The Powder Diffraction File: A quality materials characterization database. *Powder Diffr.* **2019**, *34*, 352–360. [CrossRef]
38. Rodríguez-Carvajal, J. Recent advances in magnetic structure determination by neutron powder diffraction. *Phys. B Condens. Matter* **1993**, *192*, 55–69. [CrossRef]
39. Jercinovic, M.J.; Williams, M.L.; Allaz, J.; Donovan, J.J. Trace analysis in EPMA. *IOP Conf. Ser. Mater. Sci. Eng.* **2012**, *32*, 012012. [CrossRef]
40. Jokubauskas, P. HussariX. 2024. Available online: https://github.com/sem-geologist/HussariX (accessed on 16 January 2024).
41. Mosselmans, J.F.W.; Quinn, P.D.; Dent, A.J.; Cavill, S.A.; Moreno, S.D.; Peach, A.; Leicester, P.J.; Keylock, S.J.; Gregory, S.R.; Atkinson, K.D.; et al. I18–the microfocus spectroscopy beamline at the Diamond Light Source. *J. Synchrotron Radiat.* **2009**, *16*, 818–824. [CrossRef]
42. Basham, M.; Filik, J.; Wharmby, M.T.; Chang, P.C.Y.; El Kassaby, B.; Gerring, M.; Aishima, J.; Levik, K.; Pulford, B.C.A.; Sikharulidze, I.; et al. Data Analysis WorkbeNch (DAWN). *J. Synchrotron Radiat.* **2015**, *22*, 853–858. [CrossRef]
43. Filik, J.; Ashton, A.W.; Chang, P.C.Y.; Chater, P.A.; Day, S.J.; Drakopoulos, M.; Gerring, M.W.; Hart, M.L.; Magdysyuk, O.V.; Michalik, S.; et al. Processing two-dimensional X-ray diffraction and small-angle scattering data in DAWN 2. *J. Appl. Crystallogr.* **2017**, *50*, 959–966. [CrossRef]
44. Lerotic, M.; Mak, R.; Wirick, S.; Meirer, F.; Jacobsen, C. MANTiS: A program for the analysis of X-ray spectromicroscopy data. *J. Synchrotron Radiat.* **2014**, *21*, 1206–1212. [CrossRef]
45. Liu, Y.; Meirer, F.; Williams, P.A.; Wang, J.; Andrews, J.C.; Pianetta, P. TXM-Wizard: A program for advanced data collection and evaluation in full-field transmission X-ray microscopy. *J. Synchrotron Radiat.* **2012**, *19*, 281–287. [CrossRef] [PubMed]
46. Kieffer, J.; Karkoulis, D. PyFAI, a versatile library for azimuthal regrouping. *J. Phys. Conf. Ser.* **2013**, *425*, 202012. [CrossRef]
47. Kieffer, J.; Wright, J.P. PyFAI: A Python library for high performance azimuthal integration on GPU. *Powder Diffr.* **2013**, *28*, S339–S350. [CrossRef]
48. Werner, D.; Peuker, U.A.; Mütze, T. Recycling Chain for Spent Lithium-Ion Batteries. *Metals* **2020**, *10*, 316. [CrossRef]
49. Elwert, T.; Goldmann, D.; Römer, F.; Buchert, M.; Merz, C.; Schueler, D.; Sutter, J. Current Developments and Challenges in the Recycling of Key Components of (Hybrid) Electric Vehicles. *Recycling* **2016**, *1*, 25–60. [CrossRef]
50. Träger, T.; Friedrich, B.; Weyhe, R. Recovery Concept of Value Metals from Automotive Lithium-Ion Batteries. *Chem. Ing. Tech.* **2015**, *87*, 1550–1557. [CrossRef]
51. Paulsen, J.M.; Dahn, J.R. Phase Diagram of Li−Mn−O Spinel in Air. *Chem. Mater.* **1999**, *11*, 3065–3079. [CrossRef]

52. Sasabe, M.; Asamura, A. Transport phenomenon of oxygen through molten slags. In Proceedings of the 2nd International Symposium on Metallurgical Slags and Fluxes, 1984 (2nd Int Symp Metall Slags Fluxes 1984), Lake Tahoe, NV, USA, 11–15 November 1984; pp. 651–667.
53. Schirmer, T. Stoichiometric Calculation of Lithium-Containing Phases Based on Spatially Resolved X-ray Analysis and Virtual Compounds. *Adv. X-ray Anal.* **2022**, *65*, 45–56.
54. Gaur, A.; Shrivastava, B.D. Speciation using X-ray absorption fine structure (XAFS). *Rev. J. Chem.* **2015**, *5*, 361–398. [CrossRef]